Preprint T. DeValk and R. S. Lakes, "Poisson's ratio and modulus of the gyroid lattice", Physica Status Solidi B 258 (12) 2100081 (2021). https://doi.org/10.1002/pssb.202100081

Poisson's Ratio and Modulus of the Gyroid Lattice

T. DeValk and R. S. Lakes[1,*]

[1]*Department of Engineering Physics, University of Wisconsin, Madison, WI 53706*

(Dated: July 11, 2022)

Gyroid surface lattices of different density exhibited Young's modulus consistent with stretch-dominated extremal behavior approaching the Hashin-Shtrikman upper bound. Gyroid lattices exhibited a Poisson's ratio of 0.34 ±0.06 independent of direction, independent of specimen diameter and independent of chirality. This behavior is in contrast with prior chiral lattices that exhibited pronounced size effects in Poisson's ratio, allowable for chiral elastic solids.

PACS numbers:

INTRODUCTION

Cellular solids include honeycomb, foams [1], and lattices. Honeycombs, which have a two-dimensional repeating structure, are widely used in lightweight structures; foams have a three-dimensional structure in which the cells are not identical and which do not repeat spatially. Foams comprised of rib elements are open-cell and allow flow of fluid between the cells; foams with plate or membrane elements are closed cell. As for mechanical properties, honeycomb deformation out of plane is dominated by stretch or compression of cell walls, so the modulus E varies with density ρ as $\frac{E}{E_s} = [\frac{\rho}{\rho_s}]$, in which E_s is the modulus of the solid material of which the foam is made and ρ_s is the solid density. Honeycomb deformed in plane is much more compliant than out of plane because the plate elements in the cell walls bend, $\frac{E}{E_s} \propto [\frac{\rho}{\rho_s}]^3$. Ribs in foams are bend dominated [1] so $\frac{E}{E_s} \propto [\frac{\rho}{\rho_s}]^2$. Foams of low density are therefore much less stiff than the solid material from which they are made.

Lattices have a structure that repeats in space. As with foams, lattices may contain rib elements or surface elements. Lattices made of rib elements are called rib lattices or truss lattices. The surfaces in surface lattices may be thin flat plates, which can admit simple analysis, or curved surfaces. Lattices, depending on the direction of load, may obey $\frac{E}{E_s} \propto [\frac{\rho}{\rho_s}]$ and therefore provide considerably greater stiffness than foams of the same density, made of the same solid material. Surface lattices including the gyroid were originally introduced [2–5] for their potential in structures of light weight and high stiffness and strength. The gyroid surface can be described [6] by

$$\sin 2\pi y \cos 2\pi z + \sin 2\pi z \cos 2\pi x + \sin 2\pi x \cos 2\pi y = t \quad (1)$$

with t as a constant. The gyroid lattice with $t \neq 0$ was shown to exhibit elastically chiral response [7]: an axial compression gives rise to a torsional deformation, squeeze-twist coupling. This response is nonclassical and is related to characteristic length scales in the material. If these length scales are sufficiently small, the material behaves as a classically elastic continuum. In the present research, the gyroid lattice is studied further to explore size effects in Poisson's ratio and compressive elastic modulus; also the effect of density.

The gyroid is a shell lattice with cubic structural symmetry. As with other shell lattices, its stiffness and also its strength is superior in comparison with rib lattices (also known as truss lattices) and much stiffer than foams made from the same solid material. Lattices comprised of flat plates can also offer high properties. Simple cubic plate lattices offer high properties in principal directions but they are anisotropic. Elastically isotropic plate lattices with superposed simple cubic and body centered lattices [8] have been theoretically shown to approach extremal properties at low density. However such plate lattices compartmentalize space into sealed chambers, a disadvantage in some applications. The gyroid lattice contains communicating porosity that has been exploited in biomaterials studied for tissue ingrowth [9, 10].

The gyroid lattice approaches the maximum stiffness allowed by the Hashin-Shtrikman bounds. Exact attainment of these bounds is possible in hierarchical material structures with an infinite range of length scales. For example, a hierarchical coated sphere structure with a distribution of inclusion sizes can attain the bulk modulus bound [11] and a hierarchical laminate [12] can attain the shear modulus bound. Because the gyroid does not have the complexity of a hierarchical material, its properties are particularly impressive.

The gyroid has been studied in many settings. For example, gyroids occur via self assembly [13]. They occur naturally on a fine scale in butterfly wings and give rise to color effects [14]. Optical characteristics of gyroids have been studied in vanadium pentoxide [15]. Gyroids have been observed on a fine scale in block copolymers [16, 17]. The gyroid and other periodic surfaces have been studied in the context of crystallography [18]. The gyroid structure appears in micro-emulsions [19] that exhibit phase segregation.

The gyroid lattice has cubic structural symmetry. The degree of elastic anisotropy is revealed by the Zener ratio $Z = \frac{2G(1+\nu)}{E}$ with G as shear modulus and ν as Poisson's ratio. For the gyroid with $t = 0$, $Z = 0.99$; for perfect isotropy $Z = 1$. So this gyroid exhibits elastic isotropy. With only 1% deviation, this gyroid exhibits elastic isotropy within experimental uncertainty. Elastic isotropy simplifies design and is advantageous for many applications.

MATERIALS AND METHODS

Gyroid polymer lattices were designed and prepared via additive manufacturing (3D printing). Gyroid lattices were made with a surface wall thickness of 0.4 mm and a cell size of 6 mm for cylinders. Cube specimens were made with a cell size 10 mm and different wall thickness to achieve different density. The lowest density cube had a wall thickness of about 0.6 mm.

The gyroid lattices were made as follows. The surface in Equation 1 was expressed in MATLAB. A 3D point cloud associated with the surface was extracted and was saved as a STL (stereolithography) file. Thickness was added via Blender software, and end caps for cylinders made using Solidworks software. The file was post-processed with Netfabb software for export to a EOS P760 3D printer. Cylindrical specimens were prepared with length twice the diameter; for these, the ratio of lattice density to the solid density was $\rho/\rho_s = 0.21$ for $t = 0$ and 0.195 for $t = 0.6$ and -0.6.

The solid constituent was a nylon polymer PA 2200 of density $\rho_s = 0.98$ g/cm^3, Young's modulus $E_s = 1.6$ GPa and Poisson's ratio 0.4. Gyroid cube specimens 60.5 $\pm$0.5 mm on a side were prepared with densities from 67 kg/m^{-3} to 324 kg/m^{-3}; they were non-chiral with $t = 0$. Cylindrical specimens had diameters from 11.90 mm to 41.5 mm. Cylindrical specimens were made with $t = 0$ (non-chiral), t = -0.6, and $t = 0.6$ (chiral). Representative specimens are shown in Figure 1 and 2.

Compressive load was applied at a constant rate using a 10,000 pound capacity Sintech test frame up to 1% strain in the linear domain. The deformation rate was 1.2 mm/ min corresponding to a strain rate of 3.3 $\times 10^{-4}$ /sec. Poisson's ratio of cylindrical specimens was determined from displacements obtained from digital photography. A Point Grey Research camera (GRAS-50S5M-C) was used. The camera has a resolution of 2448 x 2048 pixels, 5.0 MP total and a pixel size of 3.45 μm [20]. The camera used a Schneider-Kreuznach Xenoplan 1.9/35-0901 lens. Vic-Snap software was used to capture the pictures. The camera was moved sufficiently close that specimen image filled most of the frame, to maximize resolution. The camera was focused on ink marks made on each specimen. To deal with the resulting shallow depth of field, manual focus was used. Cameras with more pixels were tried but limitations in their focusing capability resulted in poorer images. Images were taken with focus on the marks at the front of the specimen, then on the marks on the sides, with and without compression. Deformation was obtained from the digital images with "GIMP" software. At least 20 measurements of the image points were made for each plotted data point in the Poisson's ratio graphs. Because strain was small,

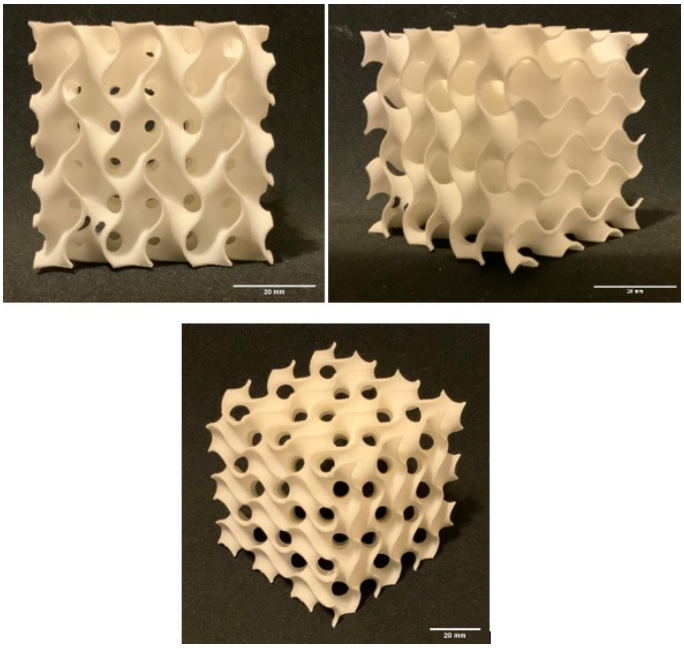

FIG. 1: Gyroid lattice cube specimens, top left, [100] direction; top right, [110] direction, bottom center, [111] direction. Scale bars: 20 mm.

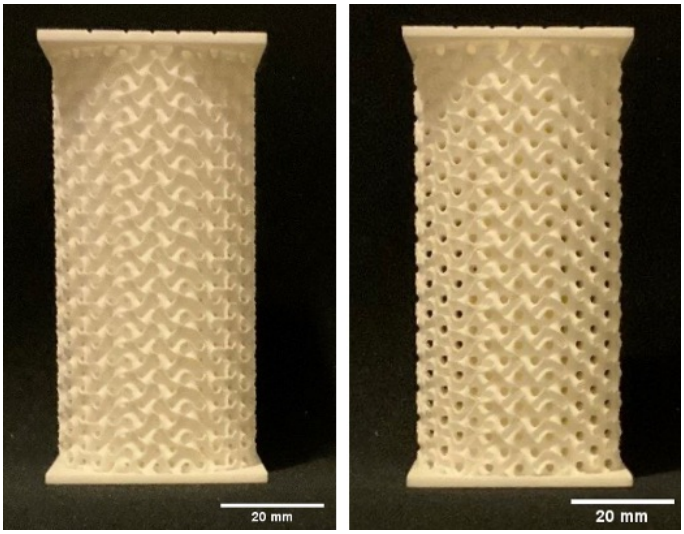

FIG. 2: Gyroid lattice cylinder specimens, left, non-chiral, right, chiral. Scale bars: 20 mm.

engineering strain was used in calculations of Poisson's ratio and modulus. The density of the cubical specimens used for the modulus studies was determined from the measured mass and dimensions of each specimen.

RESULTS

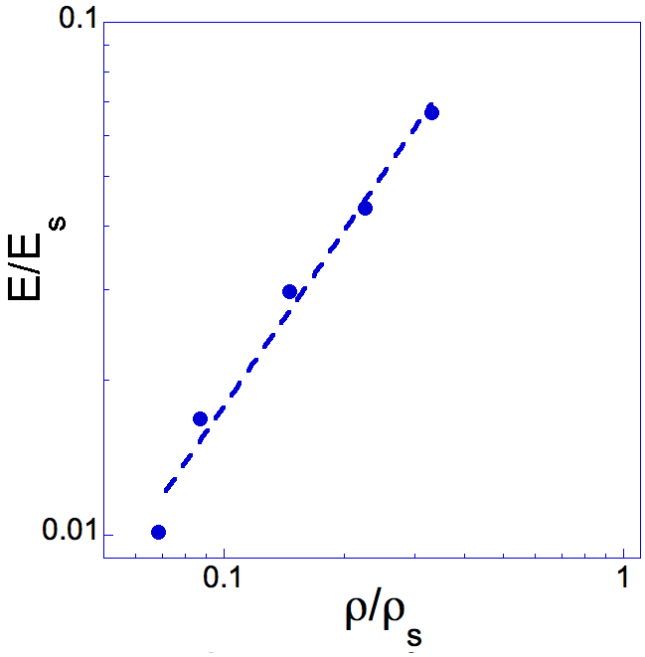

FIG. 3: Normalized Young's modulus E/E_s vs. normalized density ρ/ρ_s of non-chiral gyroid cubes. E_s is Young's modulus of the solid; ρ_s is the density of the solid.

The dependence of modulus of non-chiral gyroid cubes on density is shown in Figure 3. Young's modulus E is normalized to the modulus of the solid phase E_s, similarly the density ρ is normalized to the density of the solid phase ρ_s. A fit to all the points gave $E/E_s = 0.243\ (\rho/\rho_s)^{1.14}$ with a goodness of fit $R = 0.997$. A fit to the top four points yielded a slightly better $R = 0.9989$ with a slope of 1.014 rather than 1.14. A slope near 1 implies stretch-dominated behavior. A slope near 2 implies bend dominated behavior of rib elements [1] and is typical of foams; a slope near 3 implies bend dominated behavior of plate elements and is characteristic of honeycomb deformed in plane.

It is appropriate to compare the experimental modulus results with rigorous bounds on moduli. The bounds for two-phase composites assume isotropy and allow arbitrary phase geometry; they were developed using variational energy arguments. The lower bound for the elastic shear modulus G_L is

$$G_L = G_2 + \frac{V_1}{\frac{1}{G_1 - G_2} + \frac{6(K_2+2G_2)V_2}{5(3K_2+4G_2)G_2}}, \qquad (2)$$

in which K_1, G_1, V_1; K_2, G_2 and V_2 are the bulk modulus, shear modulus and volume fraction of phases 1 and 2, respectively. Assuming $G_1 > G_2$, then G_L is the lower bound on the shear modulus. Interchanging the subscripts 1 and 2 in Equation 2 results in the upper bound G_U for the shear modulus. Similarly the lower bound for bulk modulus is

$$K_L = K_2 + \frac{V_1(K_1 - K_2)(3K_2 + 4G_2)}{(3K_2 + 4G_2) + 3V_2(K_1 - K_2)}. \qquad (3)$$

If the material is a cellular solid such as a lattice, the lower bound is zero because one constituent is solid and the second constituent is void space. The upper bound on the bulk modulus becomes, with interchange of subscripts 1 and 2,

$$K_U = K_1 + \frac{V_2(K_2 - K_1)(3K_1 + 4G_1)}{(3K_1 + 4G_1) + 3V_1(K_2 - K_1)}. \qquad (4)$$

For a cellular solid, $K_2 = 0$ and $G_2 = 0$. The upper bound for the bulk modulus is then

$$K_U = K_1 + \frac{(1 - V_1)(-K_1)(3K_1 + 4G_1)}{(3K_1 + 4G_1) + 3V_1(-K_1)}. \qquad (5)$$

The volume fraction V_1 of the solid phase of a cellular solid is the density ratio $[\frac{\rho}{\rho_s}]$. The bulk modulus bound, expressed in terms of the solid Poisson's ratio, is shown in Figure 4.

The upper bound for the shear modulus for a cellular solid becomes

$$G_U = -\frac{1}{G_1} + \frac{(1 - V_1)}{-\frac{1}{G_1} + \frac{6(K+2G_1)V_1}{5(3K+4G_1)G_1}}. \qquad (6)$$

The shear modulus of the non-chiral gyroid lattice cylinders with $t = 0$ was found [7] via a different method to be $G = 46.8$ MPa. The shear modulus of the solid is $G_s = 577$ MPa from manufacturer values of E_s and ν_s of the parent material used for the 3D printing of the lattices. The initial slope of the Hashin-Shtrikman shear modulus bound at low density is 0.5, so the shear modulus G is 78% of the upper bound for a non-chiral gyroid of density 0.21 g/cc. These cylinders were made in only one density but different diameter and chirality in contrast to the cubes.

As for bounds, the bulk modulus of the gyroid surface lattice obtained from finite element analysis [9] approaches the upper bound on bulk modulus for Poisson's ratio = 0.2 and for low solid volume fraction. If the solid volume fraction is 0.5, the gyroid bulk modulus is

predicted to approach the upper bound as the solid Poisson's ratio tends to -1; the bulk modulus is predicted to be about 80% of the upper bound for solid Poisson's ratio 0.4. Because Young's modulus rather than bulk modulus is measured here, the comparison is indirect.

All the lattices were made by 3D printing, consequently the printed solid phase has a microstructure that differs from that of the parent material used as the feedstock. Typically, properties of the printed solid are somewhat less than those of the feedstock. It is therefore likely that the modulus / density performance of the gyroid is superior to the values inferred.

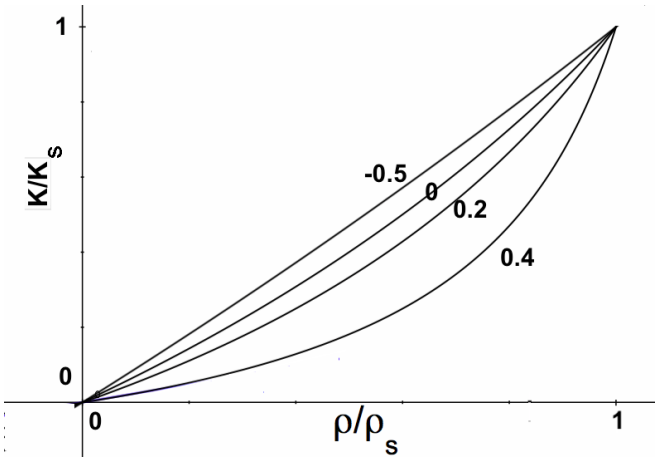

FIG. 4: Hashin-Shtrikman bounds on bulk modulus of a cellular solid for different solid Poisson's ratios (-0.5, 0, 0.2, 0.4).

Size effects in Young's modulus of gyroid cylinders are shown in Figure 5. Experimental uncertainty for the modulus measurements is comparable to the width of the data points. Size effects can occur due to distributed moments in materials considered as Cosserat solids: apparent stiffness increases as specimen size decreases. Non-chiral solids can exhibit size effects in torsion and bending but not in compression. If the solid is chiral, size effects can also occur in compression or tension. Size effects can also occur in cellular solids with incomplete cells. Incomplete cells result in a surface effect that lowers the effective modulus as specimen size decreases. Such a softening effect is evident in the thinner specimens in Figure 5. The cylinder axis corresponds to the direction [001] in the lattice.

The non-chiral gyroid cylinder was stiffer than the corresponding cube of the same density. The intersection of free surfaces at the cube edges likely amplifies the softening effect associated with incomplete cells at the surface.

Poisson's ratio is shown vs. diameter in Figure 6 for orientation in a principal direction (0° angle) and in Figure 7 for orientation in a 45° direction. Angle 0° corresponds to direction [100] in the lattice and 45° corresponds to direction [110]. Error bars represent the

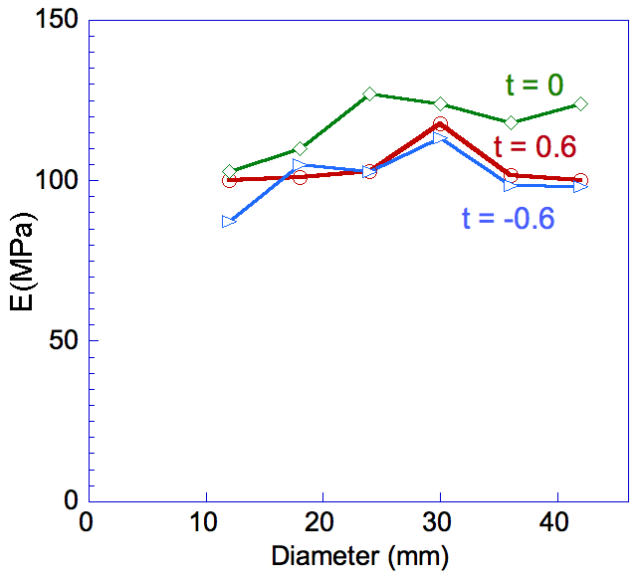

FIG. 5: Size effects in Young's modulus of gyroid cylinders. The chirality parameter is t; $t = 0$ indicates a non-chiral lattice; $t = 0.6$, -0.6 are chiral.

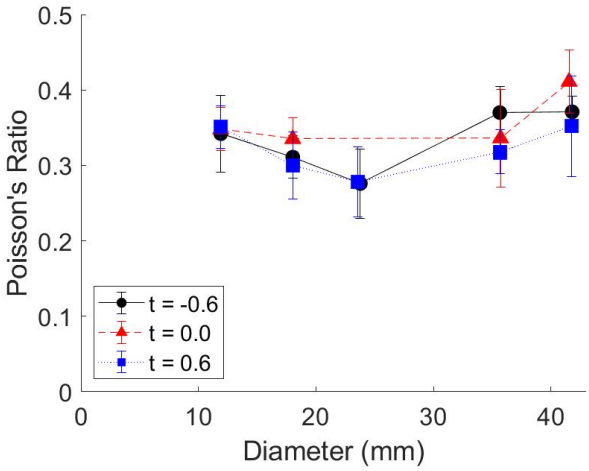

FIG. 6: Poisson's ratio vs. diameter for each chirality parameter t, 0° orientation.

standard deviation; each graph point represents the average of approximately 20 Poisson's ratio measurements. Moreover, Poisson's ratio is independent of the diameter within experimental resolution. Poisson's ratio is also independent of direction and of the degree of chirality. The average Poisson's ratio of the gyroid is 0.34 ±0.06 based on all data points. A plot of average values vs. diameter is shown in Figure 8. By contrast, designed chiral lattices [22] with oblique rib elements exhibited substantial size dependence of Poisson's ratio and also a negative Poisson's ratio for sufficiently large size. Size effects in

Poisson's ratio can occur in chiral elastic materials as predicted using Cosserat elasticity [23].

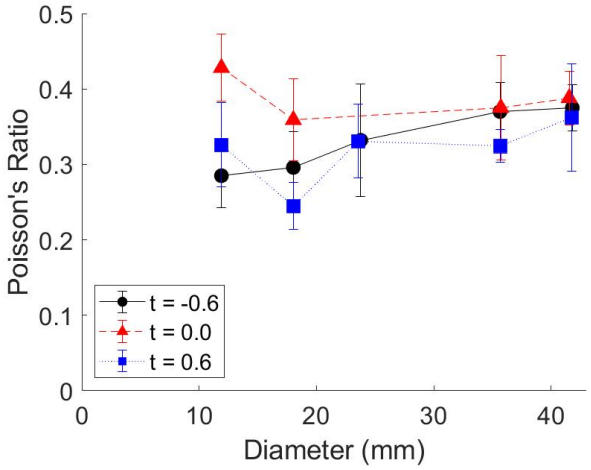

FIG. 7: Poisson's ratio vs. diameter for each chirality parameter t, 45° orientation.

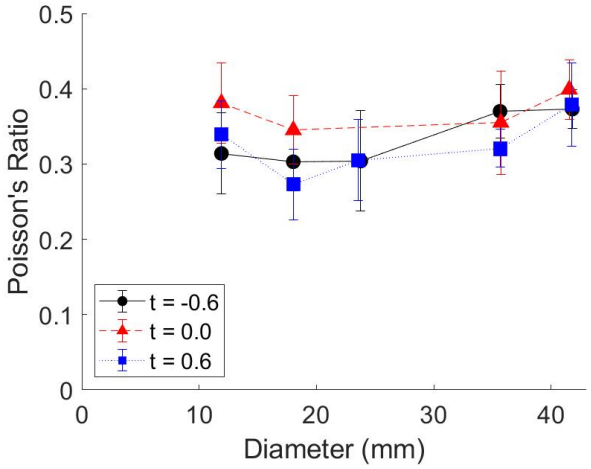

FIG. 8: Poisson's ratio vs. diameter for each chirality parameter t: average of values of the 0° and 45° results.

DISCUSSION

The gyroid is elastically isotropic based on a comparison between Young's modulus, shear modulus and Poisson's ratio [7]. In the present results, Poisson's ratio exhibited no significant dependence on direction which confirms the prior inference of elastic isotropy within the resolution of the experiments. The gyroid is a surface lattice that is stretch dominated, so the elastic modulus is linear with respect to density, not quadratic as it is in foams. Such behavior is not unique. For low density simple cubic plate lattices, $\frac{E}{E_s} = \frac{2}{3}[\frac{\rho}{\rho_s}]$; these are anisotropic [24]. Elastically isotropic plate lattices at sufficiently low density [8] approach $\frac{E}{E_s} = \frac{1}{2}[\frac{\rho}{\rho_s}]$; also stretch dominated and approaching optimal stiffness. Rib lattices of appropriate structure can be stretch dominated as well, but they are not as stiff as plate or surface lattices. Variants of cubic plate lattices can exhibit a negative Poisson's ratio, originally reported in foams [25] but via computation [26]. Such variants exhibit reduced Young's modulus.

The analysis of the modulus assumes the manufacturer quote of the modulus of the parent material. The 3D printed solid phase is usually less stiff than the parent material [27] used as feedstock. Therefore the modulus / density performance of the gyroid is likely to be superior to the values inferred and closer to the upper bound. Also, cells of the gyroid are incomplete at the surface. That can reduce the stiffness for small specimens; specimens of diameter four cells wide or less exhibited compliance due to surface effects [7]. Such surface size effects are also known in foams [28] but do not occur in lattices with complete cells. The cube specimens, which have edges with two free surfaces, may be more vulnerable to surface compliance than the cylinders. Also, as a result of limitations in 3D printing, the regime of asymptotically low density was not approached, so a comparison with analyses of that regime is precluded. The option of making the cells smaller is restricted by the resolution of the 3D printer: the cell walls at the lowest density are already rather thin. Future advances in 3D printing will permit smaller surface features and smaller cells. If the cell size is sufficiently small compared with the specimen size, the behavior will approach that of a classical elastic continuum.

The gyroid allows chirality. Chirality has long been known to play a role in chemistry and in optics however classical elasticity does not admit any effect of chirality. More freedom is required to accommodate chiral elastic deformation. Cosserat elasticity [29], also known as micropolar elasticity [30], provides sufficient freedom. Cosserat elasticity allows rotation of points as well as translation, and moment per area (couple stress) as well as the usual force per area (stress). Cosserat elasticity admits a characteristic length scale in the theory. Non-chiral Cosserat solids exhibit size effects in torsion and bending but not in tension or compression. Experiments reveal such effects in bone, foams [31, 32] and in lattices [33]. Chiral Cosserat solids are predicted to exhibit coupling between stretching or compression and twist deformation [23]. Stretch twist coupling response has been observed in bone [34] and in tendon [35] as well as in a designed cubic lattice [22] and in the gyroid lattice [7]. Analysis of chiral cholesteric elastomers [36] predicted stretch twist coupling with a characteristic length predicted to be on the order of 10 nm.

As for potential applications, periodic shell lattices in-

cluding the gyroid have been analyzed in the context of multifunctional capability such for simultaneous transport of heat and electricity [37]. As described in the introduction, the gyroid structure occurs in block copolymers and butterfly wings. The squeeze-twist coupling that occurs in chiral elastic solids including the gyroid [7] may be of use in sensors and actuators.

Chiral Cosserat solids also can exhibit nonclassical size effects in Poisson's ratio [23]. Substantial size effects were observed in the prior cubic lattice [22] but not in the present gyroid lattice. The detailed role of the nonclassical elastic constants in determining such size effects remains to be more fully delineated.

CONCLUSION

Non-chiral gyroid lattices exhibited density dependence of Young's modulus consistent with stretch-dominated behavior. The modulus is extremal and approaches the Hashin-Shtrikman upper bound. Poisson's ratio exhibited no significant dependence on direction, upon chirality, or upon specimen size.

The authors gratefully acknowledge support of this research by the National Science Foundation via Grant No. CMMI -1906890. We thank D. Reasa for preparing specimens.

* Electronic address: lakes@engr.wisc.edu; corresponding author.

[1] L. J. Gibson and M. F. Ashby, *Cellular Solids*, Pergamon, Oxford, 1988; 2nd Ed., Cambridge University press, Cambridge, (1997).

[2] A. H. Schoen, Infinite regular warped polyhedra and infinite periodic minimal surfaces. Amer. Math. Soc., Abstract 658 30, 23 30 (1968).

[3] A. H. Schoen, Infinite periodic minimal surfaces without self-intersections. NASA; Springfield, VA: Federal Scientific and Technical Information. TN D-5541 (1970).

[4] A. H. Schoen, Honeycomb panels formed of minimal surface periodic tubule layers, US Patent 3663347, (1972).

[5] A. H. Schoen, Reflections concerning triply-periodic minimal surfaces, Interface Focus 2, 658-668, (2012).

[6] M. Wohlgemuth, N. Yufa, J. Hoffman, E. L. Thomas, Triply periodic bicontinuous cubic microdomain morphologies by symmetries, Macromolecules, 34, 6063-6089, (2001).

[7] Reasa, D. R., and Lakes, R. S., Nonclassical Chiral Elasticity of the Gyroid Lattice *Physical review letters*, 125(20), 205502 (2020).

[8] T. Tancogne-Dejean, M. Diamantopoulou, M. B. Gorji, C. Bonatti, and D. Mohr, 3D Plate-Lattices: An emerging class of low-density metamaterial exhibiting optimal isotropic stiffness, Adv. Mater., 1803334 (2018).

[9] S. C. Kapfer, S. T. Hyde, K. Mecke, C. H. Arns, G. E. Schröder-Turk, Minimal surface scaffold designs for tissue engineering, Biomaterials, 32, 6875-6882, (2011).

[10] F. P. W. Melchels, K. Bertoldi, R. Gabbrielli, A. H. Velders, J. Feijen, D. W. Grijpma, Mathematically defined tissue engineering scaffold architectures prepared by stereolithography. Biomaterials 31, 6909-16, (2010).

[11] G. W. Milton and S. K. Serkov, Neutral coated inclusions in conductivity and anti-plane elasticity. Proceedings of the Royal Society 457, 1973-1997, (2001).

[12] G. W. Milton, Modeling the properties of composites by laminates. in Erickson, J. L., Kinderlehrer, D., Kohn, R., Lions, J. L. (Eds.), Homogenization and Effective Moduli of Materials and Media. Springer Verlag, Berlin, 150-175, (1986).

[13] L. J. Ellison, D. J. Michel, F. Barmes, and D. J. Cleaver, Entropy-driven formation of the gyroid cubic phase, Phys. Rev. Lett. **97**, 237801 (2006).

[14] V. Saranathan, C.O. Osuji, S. G. J. Mochrie, H. Noh, S. Narayanan, A. Sandy, E.R. Dufresne, R. O. Prum, Structure, function, and self-assembly of single network gyroid ($I\ 4_132$) photonic crystals in butterfly wing scales, Proc. Natl. Acad. Sci. USA **107**, 11676-11681 (2010).

[15] M. R. J. Scherer, L. Li, P. M. S. Cunha, O. A. Scherman, and U. Steiner, Enhanced electrochromism in gyroid-structured vanadium pentoxide, Adv. Mater. 24, 1217-1221 (2012).

[16] M. F. Schulz, FS Bates, K Almdal, K Mortensen, Epitaxial relationship for hexagonal-to-cubic phase transition in a block copolymer mixture, Phys. Rev. Lett. 73, 86-89 (1994).

[17] M. W. Matsen and M. Schick, Stable and unstable phases of a diblock copolymer melt, Phys. Rev. Lett. 72, 2660-2663 (1994).

[18] W. Fischer and K. Koch, On 3-periodic minimal surfaces, Z. Kristallogr. 179, 31-52, (1987).

[19] V. Luzzati, A. Tardieu, T. Gulek-Krzywicki, E. Rivas, F. Reiss-Husson, Structure of the cubic phases of lipid-water systems, Nature (London) **220**, 485-488 (1968).

[20] "Audio Video Supply", avsupply.com *https://www.avsupply.com/ITM/29780/GRAS-50S5M-C.html*.

[21] Z. Hashin and S. Shtrikman, A variational approach to the theory of the elastic behaviour of multiphase materials. J Mech Phys Solids, 11, 127-140 (1963).

[22] C. S. Ha, M. E. Plesha, R. S. Lakes, Chiral three-dimensional isotropic lattices with negative Poisson's ratio, Physica Status Solidi B, 253, 1243-1251 (2016).

[23] R. S. Lakes, and R. L. Benedict, Noncentrosymmetry in micropolar elasticity. Int. J. of Engng. Sci. 20, 1161-1167, (1982).

[24] R. S. Lakes, *Composites and Metamaterials*, World Scientific, (2020).

[25] R. S. Lakes, Foam structures with a negative Poisson's ratio, Science, 235 1038-1040 (1987).

[26] Searching for auxetics with DYNA3D and ParaDyn, Phys. Stat. Sol.(b) 242, 585-594 (2005).

[27] J. Quintana, A. Redmann, G. A. M. Capote, A. P. Irizarry, A. Bechara, T. Osswald, R. S. Lakes, Viscoelastic properties of fused filament fabrication parts, Additive Manufacturing, 28, 704-710, (2019).

[28] R. Brezny and D. J. Green, Characterization of edge effects in cellular materials, J. Mater. Sci., **25**, 457-4578 (1990).

[29] E. Cosserat, and F. Cosserat, *Theorie des Corps De-*

formables, Hermann et Fils, Paris (1909).

[30] A. C. Eringen, Theory of micropolar elasticity. In Fracture Vol. **1**, 621-729 (edited by H. Liebowitz), Academic Press, New York (1968).

[31] Z. Rueger and R. S. Lakes, Cosserat elasticity of negative Poisson's ratio foam: experiment, Smart Materials and Structures, **25**, 054004 (8pp) (2016).

[32] Z. Rueger and R. S. Lakes, Experimental study of elastic constants of a dense foam with weak Cosserat coupling, J. Elasticity, **137**, 101-115, (2019).

[33] Z. Rueger and R. S. Lakes, Strong Cosserat elasticity in a transversely isotropic polymer lattice, Phys. Rev. Lett., **120**, 065501 (2018).

[34] R. S. Lakes, Is bone elastically noncentrosymmetric?, Proc. 34th ACEMB. Houston (1981).

[35] K. Buchanan, R. S. Lakes, R. Vanderby, Chiral behavior in rat tail tendon fascicles, Journal of Biomechanics, **64**, 206-211 (2017).

[36] M. Warner, E. M. Terentjev, R. B. Meyer, and Y. Mao, Untwisting of a cholesteric elastomer by a mechanical field, Phys. Rev. Lett. **102**, 217601 (2009).

[37] S. Torquato, S. Hyun, A. Donev, Multifunctional composites: optimizing microstructures for simultaneous transport of heat and electricity. Phys. Rev. Lett. **89**, 266601 (2002).